



ARL-TR-7945 • FEB 2017



US Army Research Laboratory

Development of an Anatomically Accurate Finite Element Human Ocular Globe Model for Blast-Related Fluid-Structure Interaction Studies

**by Kimberly A Thompson, Rajneesh Bhardwaj, and
Thao D Nguyen**

Approved for public release; distribution is unlimited.

NOTICES

Disclaimers

The findings in this report are not to be construed as an official Department of the Army position unless so designated by other authorized documents.

Citation of manufacturer's or trade names does not constitute an official endorsement or approval of the use thereof.

Destroy this report when it is no longer needed. Do not return it to the originator.



Development of an Anatomically Accurate Finite Element Human Ocular Globe Model for Blast-Related Fluid-Structure Interaction Studies

by Kimberly A Thompson

Weapons and Materials Research Directorate, ARL

Rajneesh Bhardwaj

Indian Institute of Technology, Mumbai, India

Thao D. Nguyen

The Johns Hopkins University, Baltimore, MD

REPORT DOCUMENTATION PAGE				Form Approved OMB No. 0704-0188	
<p>Public reporting burden for this collection of information is estimated to average 1 hour per response, including the time for reviewing instructions, searching existing data sources, gathering and maintaining the data needed, and completing and reviewing the collection information. Send comments regarding this burden estimate or any other aspect of this collection of information, including suggestions for reducing the burden, to Department of Defense, Washington Headquarters Services, Directorate for Information Operations and Reports (0704-0188), 1215 Jefferson Davis Highway, Suite 1204, Arlington, VA 22202-4302. Respondents should be aware that notwithstanding any other provision of law, no person shall be subject to any penalty for failing to comply with a collection of information if it does not display a currently valid OMB control number.</p> <p>PLEASE DO NOT RETURN YOUR FORM TO THE ABOVE ADDRESS.</p>					
1. REPORT DATE (DD-MM-YYYY) February 2017		2. REPORT TYPE Technical Report		3. DATES COVERED (From - To) May–August 2013	
4. TITLE AND SUBTITLE Development of an Anatomically Accurate Finite Element Human Ocular Globe Model for Blast-Related Fluid-Structure Interaction Studies				5a. CONTRACT NUMBER	
				5b. GRANT NUMBER	
				5c. PROGRAM ELEMENT NUMBER	
6. AUTHOR(S) Kimberly A Thompson, Rajneesh Bhardwaj, and Thao D Nguyen				5d. PROJECT NUMBER	
				5e. TASK NUMBER	
				5f. WORK UNIT NUMBER	
7. PERFORMING ORGANIZATION NAME(S) AND ADDRESS(ES) US Army Research Laboratory ATTN: RDRL-WMP-B Aberdeen Proving Ground, MD 21005-5069				8. PERFORMING ORGANIZATION REPORT NUMBER ARL-TR-7945	
9. SPONSORING/MONITORING AGENCY NAME(S) AND ADDRESS(ES)				10. SPONSOR/MONITOR'S ACRONYM(S)	
				11. SPONSOR/MONITOR'S REPORT NUMBER(S)	
12. DISTRIBUTION/AVAILABILITY STATEMENT Approved for public release; distribution is unlimited.					
13. SUPPLEMENTARY NOTES					
14. ABSTRACT <p>In this report, we outline the development of an anatomically accurate, 3-D finite element model of the human eye for use in fluid-structure interaction studies to assess blast-loading effects on the Soldier. The model includes all main intraocular components: the corneo-scleral tissue shell, the lens, the zonule fibers and the ciliary body, the retina, the choroid, a detailed model of the optic nerve head), and the surrounding orbital/tissue complex. The intraocular fluid (anterior aqueous and posterior vitreous) is also included for means of fluid-structure interaction assessment.</p>					
15. SUBJECT TERMS human globe, ocular, finite element, anatomically accurate, blast loading					
16. SECURITY CLASSIFICATION OF:			17. LIMITATION OF ABSTRACT UU	18. NUMBER OF PAGES 34	19a. NAME OF RESPONSIBLE PERSON Kimberly A Thompson
a. REPORT Unclassified	b. ABSTRACT Unclassified	c. THIS PAGE Unclassified			19b. TELEPHONE NUMBER (Include area code) (410) 306-2982

Contents

List of Figures	iv
List of Tables	v
1. Introduction	1
1.1 Ocular Globe Models in the Literature	1
1.2 Model for Blast-Related Events	2
2. Full Human Ocular Globe Model	3
2.1 Generation I: Axisymmetric Model	4
2.1.1 Corneo-Scleral Shell	5
2.1.2 Lens (Cortex and Nucleus)	7
2.1.3 Zonule Fibers and Ciliary Body	9
2.1.4 Choroid and Retina	10
2.1.5 Optic Nerve Head	12
2.1.6 Aqueous and Vitreous	13
2.2 Generation II: Model with Offset ONH	14
3. Scleral Thickness Variation	16
4. Conclusion	19
5. References	20
List of Symbols, Abbreviations, and Acronyms	24
Distribution List	25

List of Figures

Fig. 1	Full axisymmetric eye model: exploded view of each component of the model, a view of the final axisymmetric model of the eye with the surrounding orbital/tissue complex, and a zoom of the cross section of the model with each component labeled	4
Fig. 2	Geometry of the full human eye, developed in Cubit 14.0, ²³ the 2-D geometry (left) revolved about the (optical) axis to give the full 3-D geometry (right)	5
Fig. 3	The corneo-scleral shell, the outer, protective shell of the eye, consists of the transparent cornea, the sclera, and the limbus. (a) 2-D geometry used for our model; geometric dimensions for this shell adopted from the model used by Stitzel et al. ¹³ (b) A 180° revolution of the geometry about the optical axis to show how the 3-D geometry was formed (vertical lines designate the necessary division of the geometry, based on internal components, for ease of meshing). (c) A quarter of the revolved finite element mesh.	6
Fig. 4	The lens used in our model includes 2 components, the outer cortex and the inner nucleus. (a) Our lens model, with dimensions shown. (b) The geometric dimensions of the lens (presented in Burd et al. ²⁶) used to develop our model. (c) Three views of the finite element mesh of our lens.	8
Fig. 5	The lens (cortex is grey and nucleus green) is attached to the shell of the eye via the zonule fibers (orange) and the ciliary body (pink). The zonule fibers are approximated in our model as one large mass for mesh simplicity. (a) The geometric model of the lens, zonule fibers, ciliary body, and anterior choroid with an image obtained from Kao et al. ³¹ to show how the ciliary body and choroid are developed. The zonule fiber attachment points to the lens are obtained from Lanchares et al. ²⁹ (b) A cross-section of the revolved finite element mesh of these anterior components.	10
Fig. 6	(a) Choroid (yellow), the vascular layer of the eye, and the retina (red), the light-sensitive inner lining of the eye. The anterior-most part of these layers are approximated with uniform thickness (retina: 0.24 mm; choroid: 0.2 mm) throughout the anterior region. (b) Large view of the layers near the ONH shown to emphasize thickness variation. (c) The literature provides approximate retinal thicknesses near the posterior pole, between the macula and scleral canal. ³³	11
Fig. 7	The ONH consists of the retina (red)/choroid (yellow) (prelaminar tissue), lamina cribrosa (orange), postlaminar neural tissue (pink), and sclera (white). (a) The geometric dimensions of the tissues that make up the ONH are given in detail in Sigal et al. ¹ (b) Our model of the ONH incorporates most of these dimensions. Thicknesses of the retina and choroid (making up the prelaminar neural tissue) are shown in Fig. 6a. (c) Finite element mesh of the ONH.	12

Fig. 8	The aqueous and vitreous humor are developed using the enclosed surfaces of all other tissue components that surround the anterior and vitreous chambers of the eye. (a) 2-D geometry of the aqueous and vitreous. (b) 3-D finite element mesh of these fluid cavities.....	14
Fig. 9	Second-generation human eye model with offset ONH: a) different views of the model and b) shows model development by assuming symmetry about the optical axis for the anterior region only. In the posterior region, the ONH is offset approximately 10° in the nasal direction.	15
Fig. 10	Second-generation human eye model with offset ONH and updated choroidal thickness from 0.3 mm in the first-generation model to 0.35 mm ⁴²	16
Fig. 11	Differences in the a) first and b) second-generation ONH models, including addition of a PLNT feature in the new model, an increased LC thickness from 0.3 to 0.45 mm, and a modified cup depth to increase element size and improve computational time	16
Fig. 12	Tissue thickness varies over the corneo-scleral shell, as shown in the literature. ^{13,24} (a and b) A study conducted by Norman et al. ²⁴ with images from normal human subjects sectioned into 15 equal-width sections along the anterior-posterior axis (12 sections of the sclera), and divided into 4 quadrants (60 total sections), over which thickness measurements were taken. (c) Our first-generation, axisymmetric model with 12 equal-width sections of the sclera (ONH to limbus). (d) Sectioning of the second-generation model where the ONH is offset to its geometrically accurately position.	17
Fig. 13	Scleral thickness variation procedure in the model: a) scleral thickness variation contours with thickness values noted from Norman et al., ^{3,24} b) different views of scleral thickness variation contours, and c) views of the scleral thickness before and after interpolation was implemented.....	18

List of Tables

Table 1	The coefficients for the fifth-order polynomial used to describe the lens outline. The anterior and posterior curves of the lens have different curvatures and are therefore described using different polynomial coefficients (a–f).....	8
---------	---	---

INTENTIONALLY LEFT BLANK.

1. Introduction

This report takes a detailed look into the development of an anatomically accurate, 3-D finite element model of the human ocular globe for use in studies to assess blast loading effects and subsequent injury to the eye of the Soldier. This model includes the following: the corneo-scleral shell and limbal intersection; the lens, connected to the scleral wall by way of the zonule fibers and the ciliary body; the retina; the choroid (vascular layer of the eye); a detailed model of the optic nerve head (ONH) with accurate representation of the pre- and postlaminar neural tissues and lamina cribrosa, and the surrounding orbital/tissue complex. The intraocular fluid (anterior aqueous and posterior vitreous) is also included for means of fluid-structure interaction assessment.

1.1 Ocular Globe Models in the Literature

Computational models of the eye have been developed for epidemiological studies as well as the study of injury caused by low- and high-rate loading to the eye itself. Depending on the focus of the study, the model will likely differ. When developing a model to study a specific disease, the focus may lie more in the component of interest. For example, to study glaucoma, damage to the optic nerve due to increased intraocular pressures, a model may be highly refined around the ONH but less refined in other regions of the eye.¹⁻⁸ For studying keratoconus, a thinning disorder of the cornea, a model of the cornea itself is likely sufficient,^{9,10} and for studies of myopia, or nearsightedness, the model may focus more on the cornea, lens, and retina, controlling the focusing power of the eye.

Several models also exist for evaluating the effects of impact loading on the eye. A majority of the studies have focused on blunt, or projectile, impact loading in particular, commonly resulting from a range of sporting injuries, automobile crashes, and select military-related injuries. Such models typically encompass the entire ocular globe, though often they may have more-refined components in regions where injury is known or assumed to occur. Liu et al.¹¹ determined that retinal detachment is among the injuries that result from traumatic blunt impact to the eye. Their model includes a refined retina, with varying thicknesses through the posterior region, and more-simplified versions of all other intraocular components. Uchio et al.¹² developed a model of the human eye to simulate projectile impacts, using shell elements for the corneo-scleral shell and all main intraocular components and using solid elements for the aqueous and vitreous humor. They performed uniaxial strip tests of corneal and scleral tissue to incorporate the constitutive response of these tissues in the model. By creating a quarter-symmetric

model, Stitzel et al.¹³ assessed globe rupture from foam particle, BB-gun pellet, and baseball projectile loading to only the center of the eye. Other models include the orbit and extraocular tissues as well. Power¹⁴ investigated ocular injuries to helicopter pilots from night-vision goggles, incorporating a bony orbit with fatty tissue and the 6 muscles' co-movement. Schutte et al.¹⁵ developed a model of the human eye from magnetic resonance imaging (MRI), also including the orbital structure, 4 rectus muscles, and surrounding fatty tissue, to study the complex orbital biomechanics associated with ocular motility and suspension under torsional forced duction tests.

Blast-related ocular injuries have become more prevalent in recent years due to improvised explosive devices used in the wars in Afghanistan and Iraq. Groups have used finite element models to investigate the effects of primary blast wave loading on the eye. Watson et al.¹⁶ evaluated primary blast wave insult through a combined experimental-computational approach using a porcine eye. They noted that peak stresses in the eye model were aligned with damage observed in the experiments. Rossi et al.¹⁷ modeled the human eye with surrounding tissue and orbit, exposing it to a blast wave by means of a simulated detonation. They concluded that the pyramid-like shape of the surrounding bony orbit and the impedance mismatch between the stiff orbit and softer ocular tissues caused wave reflections and pressure amplifications under blast loading. Esposito et al.¹⁸ used a similar eye model as Rossi et al.¹⁷ and analyzed pressures developed from blast exposure at the retinal macula, the base of the vitreous humor, and the orbital apex. Their results also emphasized these wave reflections they predicted could potentially be harmful to the ocular tissues.

1.2 Model for Blast-Related Events

A blast-related event can lead to primary, secondary, tertiary, and quaternary injuries.¹⁹ The primary injury is due to the blast wave itself, the over-pressurized impulse of the detonation. Secondary injuries result from airborne fragments or debris from the explosion. Tertiary injuries are due to the body being thrown by the over-heated airflow that follows the initial over-pressure of the blast wave, while quaternary injuries distinguish all remaining injuries.¹⁹

A majority of ocular combat injuries are secondary in nature, resulting from propelled fragments or blunt force trauma. Such injuries have been studied for decades, as noted in Section 1.1. Although interest has escalated more recently to determine the mechanism of the injury ensued by the primary blast wave itself, more research and evidence is necessary to reach a definitive conclusion.

This report outlines the detailed development of a finite element model of the human eye for use in fluid-structure interaction studies^{20–22} to understand the effects of ocular blast-related events on the Soldier. Such studies, focusing on the primary blast wave in particular, are carried out using a loosely coupled fluid-structure interaction solver, where fluid flow is followed across an Eulerian grid to capture pressures of the blast wave to apply as a boundary condition for the solid phase. The solid phase is tracked using a Lagrangian framework that provides velocities that are fed back to the flow solver, in a sequential manner, as deformation progresses. These studies provide insight to the interaction between the stiff, fibrous ocular tissues and the softer internal ocular structures. We suspect that injuries to the corneo-scleral shell as well as the intraocular components can result from distortional deformation of the full globe as well as an increase in intraocular pressure in the anterior and posterior chambers when the blast wave hits the eye and reflects off of stiffer surrounding facial features. As a result, because of the uncertainty of the mechanical response of all tissue within the globe, our model includes detailed characterization of all intraocular components of the human eye. Any simplifications made are noted in the text.

Several challenges arise when creating a structured, soft-tissue finite element model for exposure to high-pressurized blast loading conditions, such as maintaining a balance between an accurate geometry and a manageable computation time. Considering length and time scales associated with high-rate loading events as well as mesh quality for large deformation of nonlinear materials is also important. These were assessed and accounted for throughout the development of this model.

2. Full Human Ocular Globe Model

The full eye model is developed from averaged anatomic measures obtained from a combination of different methods described in the literature (specified in the following tissue sections). These anatomic measures are obtained from individuals in the age range consistent with that of the average Soldier (20–30 years). Two generation models are developed. While both models contain the same detailed intraocular components, the first-generation model is an axisymmetric model; axisymmetric about the optical axis (anterior-posterior). The second-generation model incorporates a more accurate representation of the ONH placement, offset from the optical axis. Development of this model is more difficult, as the posterior region of the ocular globe cannot assume symmetry about the central axis but is necessary to assess the mechanical loading effects on the eye with an offset optical nerve. Both models are shown, and all intraocular components are outlined in this report.

2.1 Generation I: Axisymmetric Model

An axisymmetric model of the full human eye was developed as a first-generation model, shown in Fig. 1. In this model, the ONH sits along this optical axis for simplicity. This allows all intraocular components to be developed assuming symmetry. This is a common assumption in the literature.^{3,11,13}

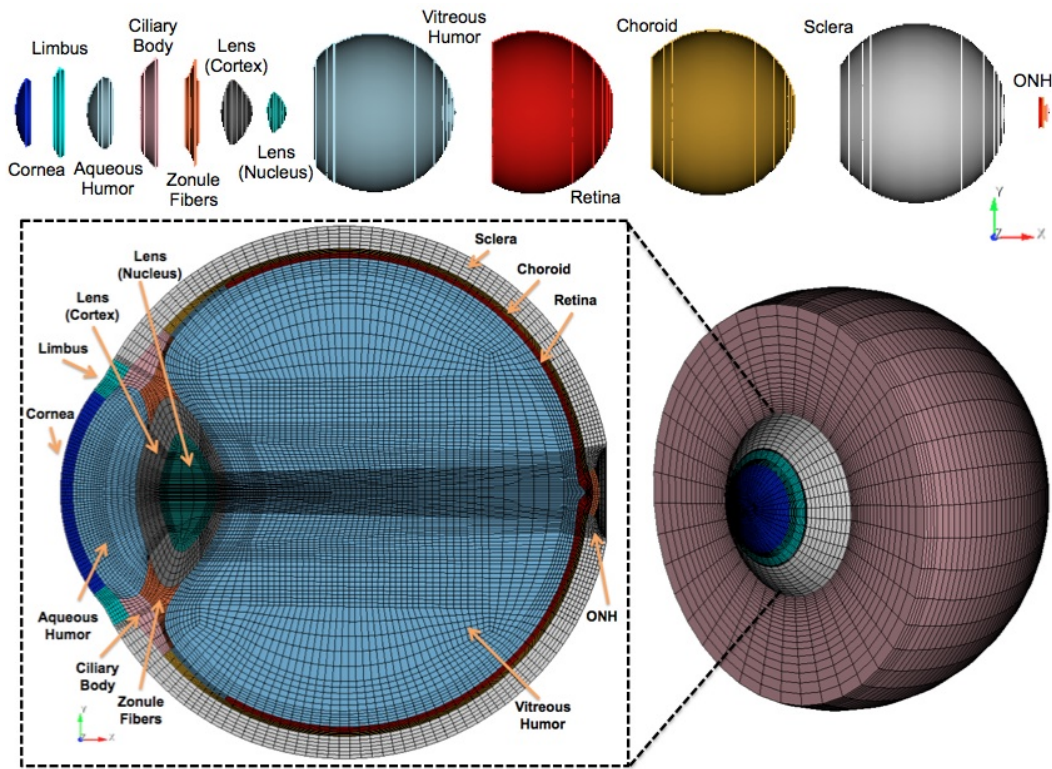


Fig. 1 Full axisymmetric eye model: exploded view of each component of the model, a view of the final axisymmetric model of the eye with the surrounding orbital/tissue complex, and a zoom of the cross section of the model with each component labeled

Every component of this model was carefully constructed by hand in Cubit 14.0,²³ a geometry and mesh generation software package developed at Sandia National Laboratories, starting with a 2-D cross-sectional geometry (Fig. 2). This cross section was then revolved about the optical axis (Fig. 2) to give an axisymmetric 3-D geometry similar to the approach taken by Stitzel et al.¹³

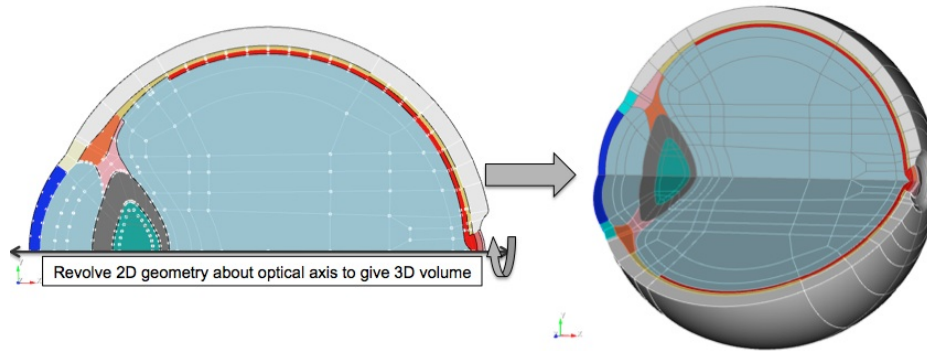


Fig. 2 Geometry of the full human eye, developed in Cubit 14.0,²³ the 2-D geometry (left) revolved about the (optical) axis to give the full 3-D geometry (right)

The geometry was created starting with the outer corneo-scleral shell and working inward, finishing with the aqueous and vitreous humor in the anterior and vitreous chambers, respectively. The anterior chamber is the region between the cornea and the iris. However, the iris is not included in our model because we assume that it will have negligible mechanical effect under blast loading; therefore, we refer to the anterior chamber as the space between the cornea and the lens. The vitreous, as it is typically referred to, is the space between the lens and the retina. Aside from the outer shell, a vertex-spline procedure was used to develop each component separately, approximating geometries from different measurements provided in the literature. The geometry is divided within each component, as shown by line segmentation in Fig. 2, to ensure good quality hexahedral elements could be developed from the spherical shape of the eye. After geometry development, a structured, finite element mesh was created with linear, hexahedral elements one tissue component at a time to ensure coherent boundaries of each adjacent component and to ensure high-quality elements. Nodes are shared between each component in the model.

2.1.1 Corneo-Scleral Shell

The corneo-scleral shell is the outer, protective layer of the eye. It consists of the transparent cornea, the opaque sclera, and the limbus that serves as the intersection between the cornea and sclera, all of which are highly fibrous tissue layers. The shape and dimensions for this shell were adopted from the model used by Stitzel et al.¹³ For example, the outer curves of the 2-D geometry for the cornea and sclera were created from circles of radius 7.8 and 12 mm, respectively, offset by 5 mm, as shown in Fig. 3. The inner curves were then created, taking into account the thickness variation for each tissue, and finally 2-D surfaces were developed by linking these curves for each respective tissue. In Figure 3a, the posterior sclera terminates where the ONH resides. The ONH is described in more detail in Section 2.1.5.

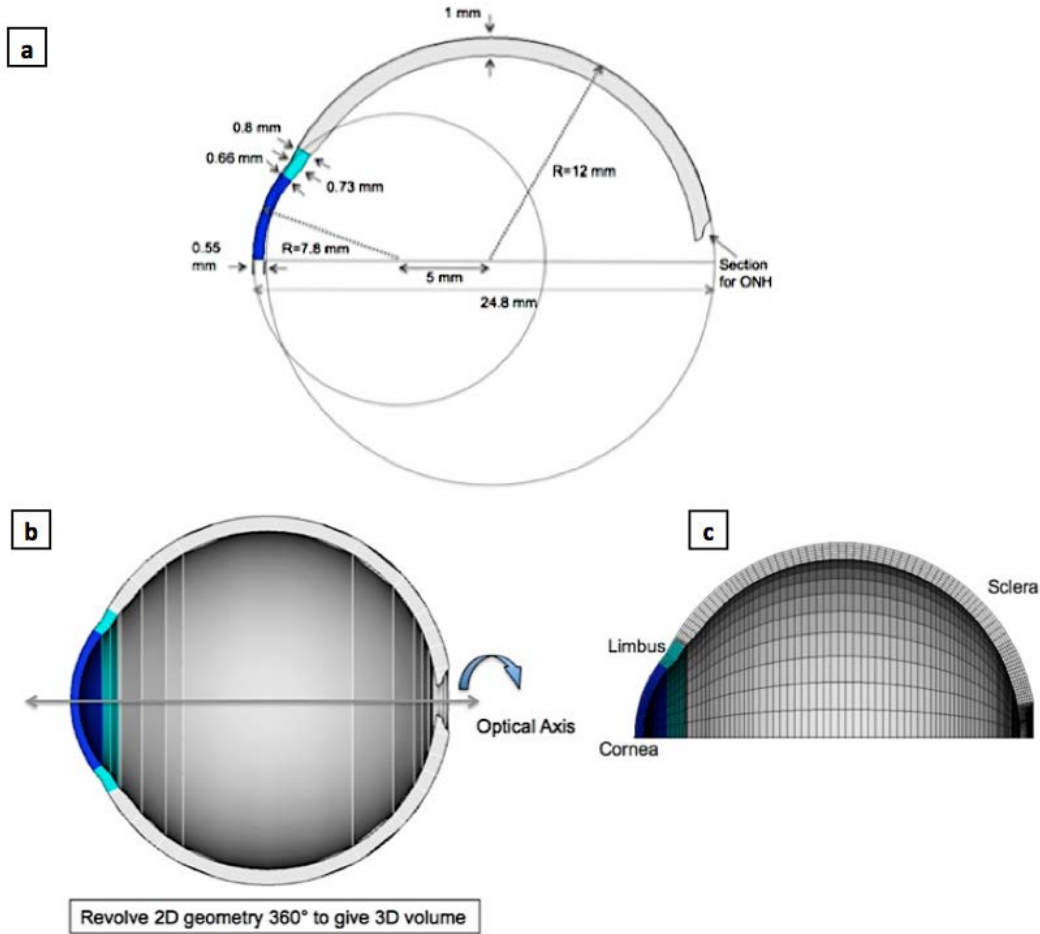


Fig. 3 The corneo-scleral shell, the outer, protective shell of the eye, consists of the transparent cornea, the sclera, and the limbus. (a) 2-D geometry used for our model; geometric dimensions for this shell adopted from the model used by Stitzel et al.¹³ (b) A 180° revolution of the geometry about the optical axis to show how the 3-D geometry was formed (vertical lines designate the necessary division of the geometry, based on internal components, for ease of meshing). (c) A quarter of the revolved finite element mesh.

The cornea, limbus, and sclera were all created as separate components due to their differences in fibrous structure and mechanical response. The thickness of the central cornea was chosen to be slightly different than that used in Stitzel et al.¹³ based on data gathered from other sources.²⁴ Rather than a thickness of 0.52 mm , a thickness of 0.55 mm was used. The limbus was created assuming a gradual change from the end of the cornea (0.66 mm) to the start of the sclera (0.8 mm), providing a central thickness of the limbus of 0.73 mm . In reality, the thickness of the sclera varies from anterior to posterior as well as across quadrants (nasal, temporal, superior, and inferior). During model development we assumed a uniform thickness of the scleral shell (1 mm), for simplicity. Upon completion, the model was manipulated to account for scleral thickness variation as described in Section 3.

2.1.2 Lens (Cortex and Nucleus)

The human crystalline lens is a transparent component in the anterior segment of the eye that divides the anterior and vitreous chambers. It is a biconvex structure that aids in refracting the light that enters the pupil onto the retina. The optical power of the eye is adjusted by changing the shape of the lens in the normal, young human eye.²⁵ Images, both near and far, can be focused on the retina through a process known as accommodation. The zonule fibers, attached to the periphery of the lens, are passive in nature, controlled by the ciliary muscle. If left alone, the fibers will naturally try to pull the lens to flatten it. When focusing on objects at a distance, the ciliary muscle relaxes and the zonule fibers naturally pull the lens in tension. This causes the lens to become flattened and more oval in shape.²⁵ When focusing on near objects, the ciliary muscle contracts, allowing the natural tension in the zonule fibers to be minimized. This causes the anterior-posterior distance of the lens to increase as the lens approaches a more spherical shape. The latter is the state of the “accommodated” lens.²⁵

In considering blast events, the time scale is on the order of a few milliseconds. The difference in thickness and shape of the lens, from the unaccommodated state to the accommodated state, is small (microns) compared with the length scale of the full human eye (centimeters) over which we are measuring fluid-structure interactions. Therefore, we are not concerned with modeling differences in accommodation. As a result, we have chosen to approximate the geometry of the lens using data from a young, normal, accommodated lens as described in Burd et al.,²⁶ as the majority of data provided in the literature is for the accommodated lens.

The lens in our model includes 2 components, the outer cortex and the inner nucleus, because the cortex is roughly 3 times stiffer than the nucleus.²⁷ Similar to the corneo-scleral shell, we assume that the lens is axisymmetric about the optical axis, which is a common assumption made in the literature.^{3,11,13} As a result, we developed a 2-D geometry of the lens as shown in Fig. 4. The geometric dimensions of the cortex are based on the approach presented in Burd et al.²⁶ The following fifth-order polynomial is used to define the cortex outline (coefficients chosen for a 29-year-old lens):

$$y=ax^5+bx^4+cx^3+dx^2+f, \quad (1)$$

where x and y are shown in Fig. 4a and the coefficients for both anterior and posterior lens outlines are provided in Table 1. This polynomial is used to define the outline of the lens from the central axis to the designated points shown in Fig. 4a (blue points). The periphery of the lens is developed by joining these anterior and posterior points with a circular end cap,²⁶ also shown in Fig. 4a.

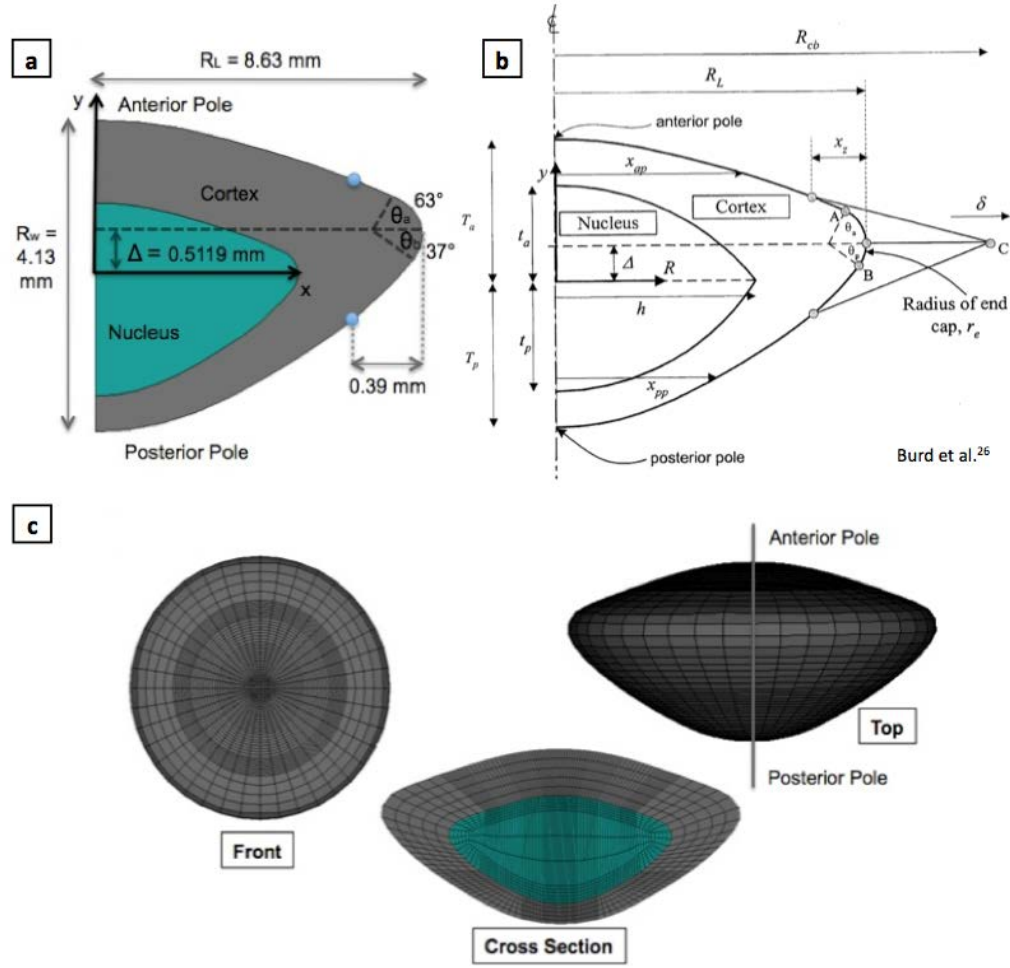


Fig. 4 The lens used in our model includes 2 components, the outer cortex and the inner nucleus. (a) Our lens model, with dimensions shown. (b) The geometric dimensions of the lens (presented in Burd et al.²⁶) used to develop our model. (c) Three views of the finite element mesh of our lens.

Table 1 The coefficients for the fifth-order polynomial used to describe the lens outline. The anterior and posterior curves of the lens have different curvatures and are therefore described using different polynomial coefficients (a–f).

Lens curve	a	b	c	d	f
Anterior	-0.0015.0045	0.011911115	-0.020325621	-0.076923077	2.04
Posterior	0.003755587	-0.030365163	0.069554836	0.094339623	-2.09

In our model, different than that in Burd et al.,²⁶ we developed the nucleus using the same shape as the cortex but scaled it down such that the thickness of the nucleus is a percentage of the total central thickness of the lens (~62%), similar to the approach taken by Schachar et al.²⁸ (using data for the accommodated 20-year-old lens). We then offset the horizontal axis of the nucleus from that of the outer cortex by 0.5119 mm as described by Burd et al.²⁶

2.1.3 Zonule Fibers and Ciliary Body

As noted, the lens is attached to the outer shell of the eye by means of the zonule fibers and the ciliary body. This lens/zonule fiber/ciliary body complex acts as the barrier between the anterior and vitreous chambers and therefore the aqueous and vitreous humor. This is important to our model in that it will assist in providing insight into internal wave propagation mechanisms in fluid-structure interaction studies.

The zonule fibers in the human eye can be, and have throughout the literature, divided into 3 separate bundles (anterior, central, and posterior), as the stiffness of each is different. The anterior zonules are 2 times the stiffness of the posterior fibers, which in turn are 3 times stiffer than the central fibers.²⁶ In our model the fibers are approximated as one large mass for mesh simplicity (Fig. 5, orange). The anterior attachment location (Fig. 5a) of the zonule fibers to the lens, 1.5 mm from the lens periphery, was adopted from Lanchares et al.²⁹ The posterior location, in relation to the lens periphery, was modified (decreased) from that provided in Lanchares et al.²⁹ for mesh quality purposes (e.g., element aspect ratio). The general location where the zonule fibers attach to the ciliary body was chosen based on Bernal et al.³⁰

The ciliary body is a complex structure including the ciliary muscle and ciliary processes. Due to the length scale of our full eye model, versus that of the individual ciliary processes, we modeled the ciliary body as a lumped mass (Fig. 5, pink). The geometry, location, and varying thickness of the ciliary body, from anterior to posterior, was adopted from Kao et al.³¹ Through comparison of images and models in the literature, we made the assumption that the ciliary body merges directly into the choroid, approximately 3 mm anterior to the ora serrata, the anterior-most region of the retina. We assumed a uniform thickness of 0.2 mm for the choroid posterior to the ora serrata and anterior to the scleral canal. As shown in Fig. 5a, we used a smooth, linear transition for the choroidal thickness from that of the ciliary body where the thickness is 0.42 mm to the ora serrata where the thickness is 0.2 mm.

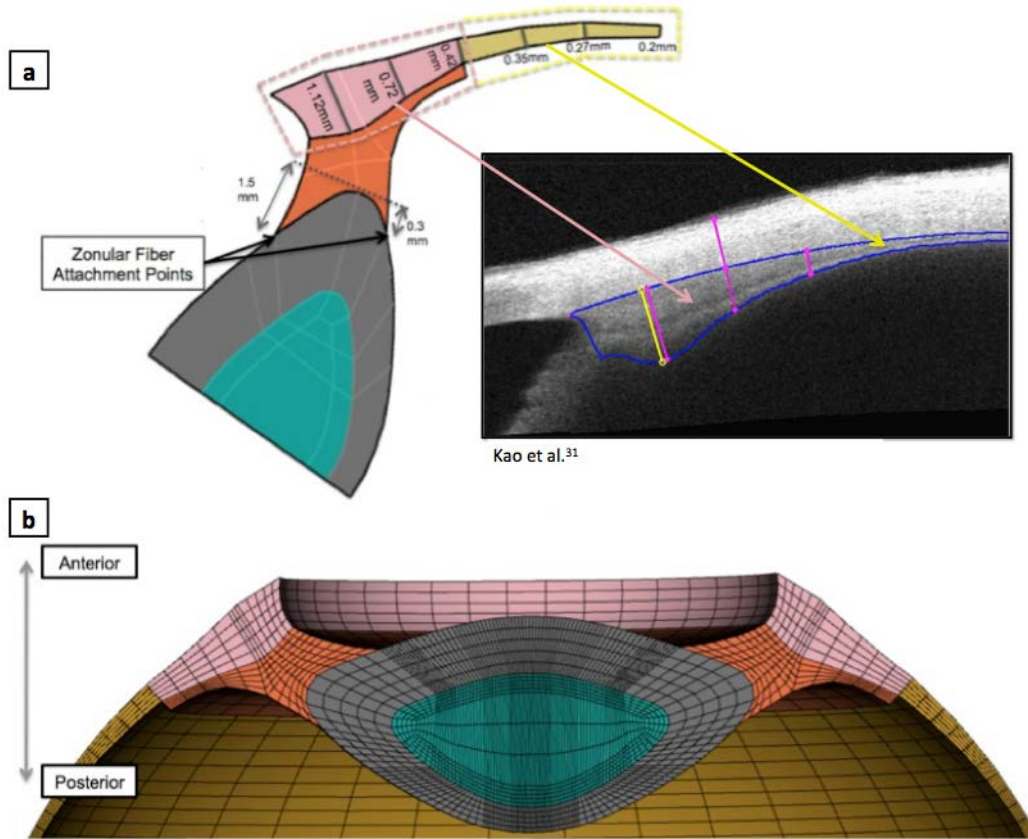
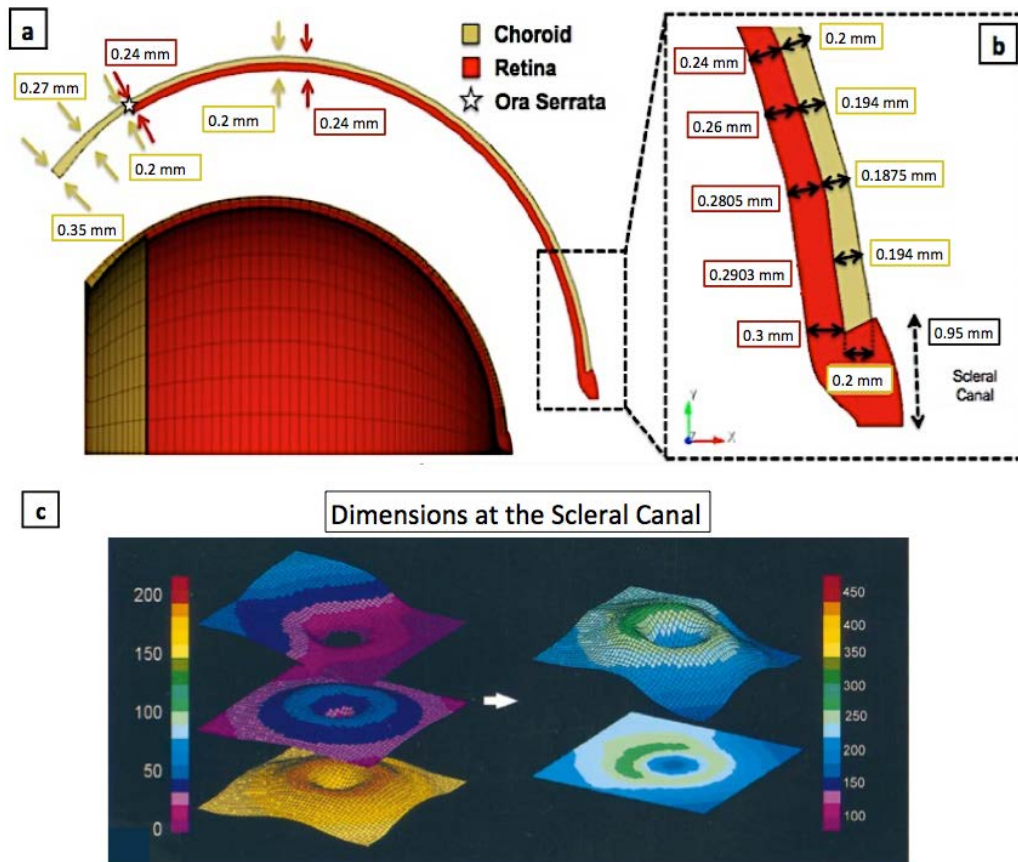


Fig. 5 The lens (cortex is grey and nucleus green) is attached to the shell of the eye via the zonule fibers (orange) and the ciliary body (pink). The zonule fibers are approximated in our model as one large mass for mesh simplicity. (a) The geometric model of the lens, zonule fibers, ciliary body, and anterior choroid with an image obtained from Kao et al.³¹ to show how the ciliary body and choroid are developed. The zonule fiber attachment points to the lens are obtained from Lanchares et al.²⁹ (b) A cross-section of the revolved finite element mesh of these anterior components.

2.1.4 Choroid and Retina

The choroid is the vascular layer of the eye (Fig. 6, yellow), and the retina is the light-sensitive inner lining of the eye (Fig. 6, red). The choroid lines the interior surface of the sclera, posterior to the ciliary body, while the retina lines the interior surface of the choroid, posterior to the ora serrata (Fig. 6a). As described in Section 2.1.3, the choroid reaches from the posterior end of the ciliary body to the scleral canal wall near the ONH. Anterior thickness measurements for the choroid (Fig. 5a) are determined by calculating incremental distances along the image in Kao et al.³¹ using ImageJ software. The retina begins at the ora serrata, which is approximately 120° from the optical axis (the axis of symmetry in the first-generation model), and terminates at the ONH.³² As shown in Fig. 6a, the choroidal and retinal layers are approximated with a uniform thickness (choroid: 0.2 mm; retina: 0.24 mm) between the ora serrata and the macula.



Asrani et al.³³

Fig. 6 (a) Choroid (yellow), the vascular layer of the eye, and the retina (red), the light-sensitive inner lining of the eye. The anterior-most part of these layers are approximated with uniform thickness (retina: 0.24 mm; choroid: 0.2 mm) throughout the anterior region. (b) Large view of the layers near the ONH shown to emphasize thickness variation. (c) The literature provides approximate retinal thicknesses near the posterior pole, between the macula and scleral canal.³³

The macula is an oval-shaped region in the retina with an approximate diameter of 6 mm and a few millimeters offset from the center of the ONH.^{34–36} Manjuath et al.³⁷ provides detailed analysis on the variation of choroidal tissue thickness at the fovea, the central region of the macula, and up to 2.5 mm beyond the fovea. Similar analysis is provided for the retinal thickness variation.^{34–36} To maintain the axisymmetric shape of the eye, this model does not include the macula/foveal pit in the retina.

Although we did not model the actual macula at this time, we did vary the thickness of the retinal and choroidal tissues in the region surrounding where the macula would be located, up to the ONH (Fig. 6b). We used a smooth, linear transition in tissue thickness, as approximated in the literature. At the scleral canal, roughly 0.95 mm from the center of ONH,¹ the retinal and choroidal thicknesses (retina: 0.3 mm; choroid: 0.2 mm) were also chosen based on values provided in the literature.^{33,38,39}

2.1.5 Optic Nerve Head

The ONH consists of the retina, the choroid, the lamina cribrosa (LC), the neural tissue, and the sclera (Fig. 7a). The geometric dimensions of the tissues that make up the ONH are given in detail in Sigal et al.¹ Our model of the ONH incorporates most of the baseline dimensions provided in Sigal et al.¹ (Fig. 7b), including peripapillary rim height, cup depth, cup shape, tissue thicknesses at the canal and axis, canal wall angle, LC anterior surface radius, and laminar curvature. Thicknesses of the retina and choroid, comprising the prelaminar neural tissue at the scleral canal wall, are adopted from other sources,^{33,38,39} as described in Section 2.1.4 and shown in Fig. 6.

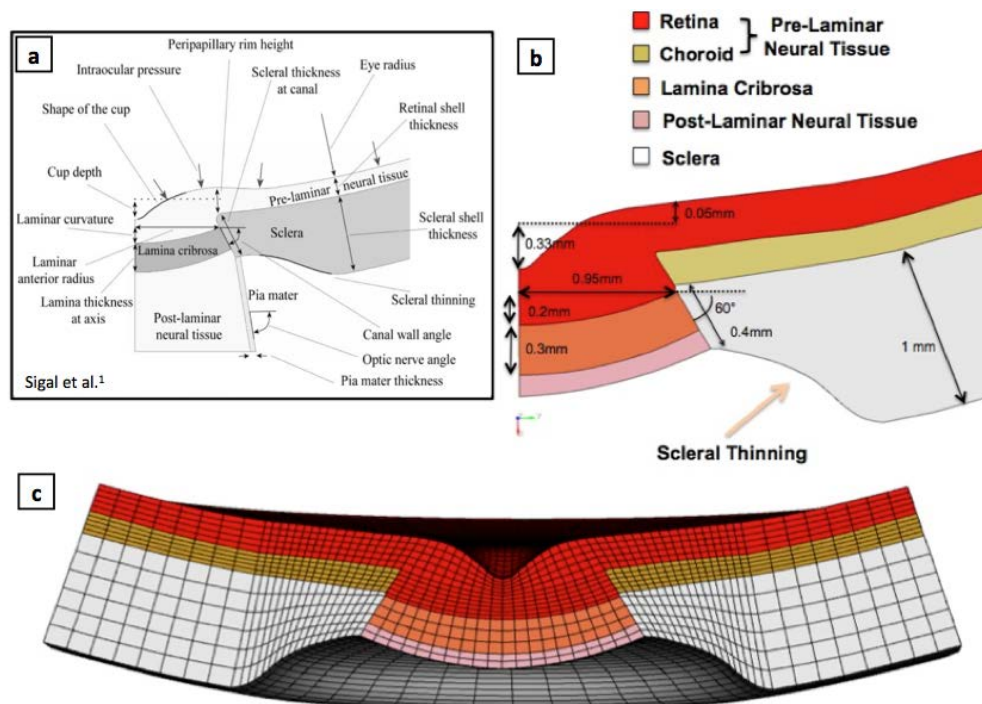


Fig. 7 The ONH consists of the retina (red)/choroid (yellow) (prelaminar tissue), lamina cribrosa (orange), postlaminar neural tissue (pink), and sclera (white). (a) The geometric dimensions of the tissues that make up the ONH are given in detail in Sigal et al.¹ (b) Our model of the ONH incorporates most of these dimensions. Thicknesses of the retina and choroid (making up the prelaminar neural tissue) are shown in Fig. 6a. (c) Finite element mesh of the ONH.

As provided by Sigal et al.,¹ the sclera is approximately 0.4 mm in thickness at the scleral canal wall and gradually increases to 1 mm where it remains for a portion of the posterior sclera before gradually decreasing again toward the equator. This thickness variation over the entire sclera is shown in detail in Norman et al.,²⁴ as

described in Section 3. Sigal et al.¹ refers to this transition of the sclera as it decreases to 0.4 mm at the canal wall as “scleral thinning”. We approximated this gradual transition using a third-order polynomial,

$$y = 15x^3 - 13x^2 + 4.8x + 0.01, \quad (2)$$

to best match the image provided in Sigal et al.¹ (Fig. 7a). The LC is a highly fibrous tissue at the cup of the ONH. Its thickness at the central axis of the ONH is 0.3 mm.¹ We developed the shape of the LC using the curvature, radius, and thickness provided by Sigal et al.¹ The shape of the ONH cup was created using the cup depth and the cup depth “reference level”, as described by Sigal et al.¹ This reference level is shown as the dotted line in Fig. 7a and is 0.05 mm from the tip of the peripapillary rim. With these dimensions and using a smooth cup-like transition to approximately match that shown in the model by Sigal et al.,¹ the current shape of the cup was formed. Because of the small length scale of this cup depth, compared with that of the full eye, we may not see a significant change in the fluid-structure interaction results if we vary the cup depth and shape. Thus, we assume this geometry is a reasonable approximation. Posterior to the LC, we provide a small region for the postlaminar neural tissue, which is simply a continuation of the surrounding fatty tissue. This tissue is very compliant compared with the adjacent tissues of the eye.

2.1.6 Aqueous and Vitreous

The aqueous and vitreous humor (Fig. 8) are the fluids that fill in the anterior and vitreous chambers of the human eye, respectively. Both fluids are transparent. While the vitreous is a gel-like fluid, the aqueous is closer to a water-like substance, with a smaller shear modulus. These fluids are developed after the geometries of the all-encompassing tissue components are created. They are simply created using the enclosed surfaces of all other tissue components that surround the anterior and vitreous chambers of the eye.

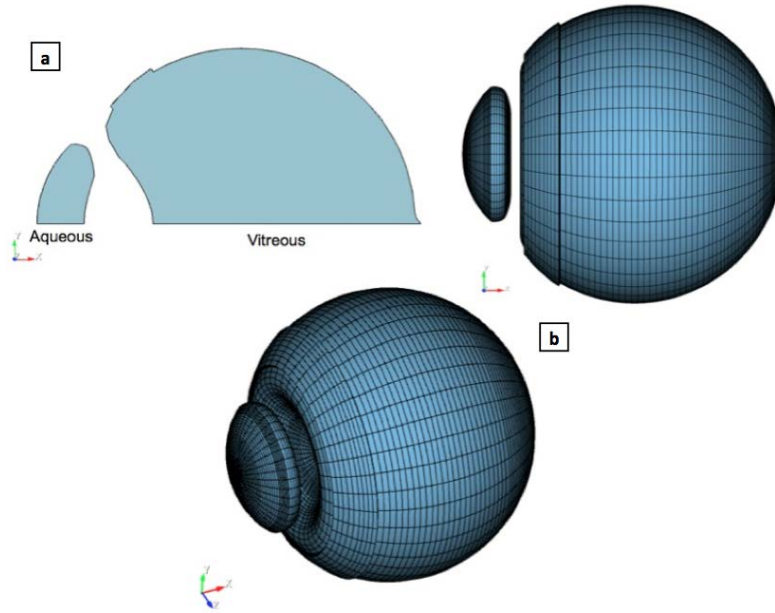


Fig. 8 The aqueous and vitreous humor are developed using the enclosed surfaces of all other tissue components that surround the anterior and vitreous chambers of the eye. (a) 2-D geometry of the aqueous and vitreous. (b) 3-D finite element mesh of these fluid cavities.

2.2 Generation II: Model with Offset ONH

As noted in Section 2, 2 models were developed. The first-generation model assumed that the full human globe is axisymmetric. However, in reality, the ONH does not sit along the geometric, optical axis. The fovea (not included in our model), which sits along the visual axis, is located approximately 5° to the temporal side and 1.5° to the inferior side of the optical axis.⁴⁰ The ONH is located roughly 15° to the nasal side and 1.5° to the superior side of the fovea.⁴¹ Thus, the ONH sits approximately 10° to the nasal side of the optical axis rather than along the optical axis as approximated in the first-generation model.

To improve the accuracy of the first model, a second-generation model was developed with an offset ONH, as shown in Fig 9. The anterior region of the eye model, up to the approximate start of the retina as well as the orbital/tissue complex, was developed in the same manner as the first-generation model, assuming symmetry about the optical axis. The ONH was created in the same manner as well and then rotated to the appropriate location. Through a series of lofted surfaces in Cubit 14.0,²³ the posterior region surrounding the ONH was created and connected to the anterior axisymmetric region. Mesh densities were chosen to ensure high-quality elements in smaller intraocular components to accurately represent the geometry, as was done in the first-generation model. In the larger vitreous chamber and fatty tissue regions, elements were gradually increased to help minimize computation time.

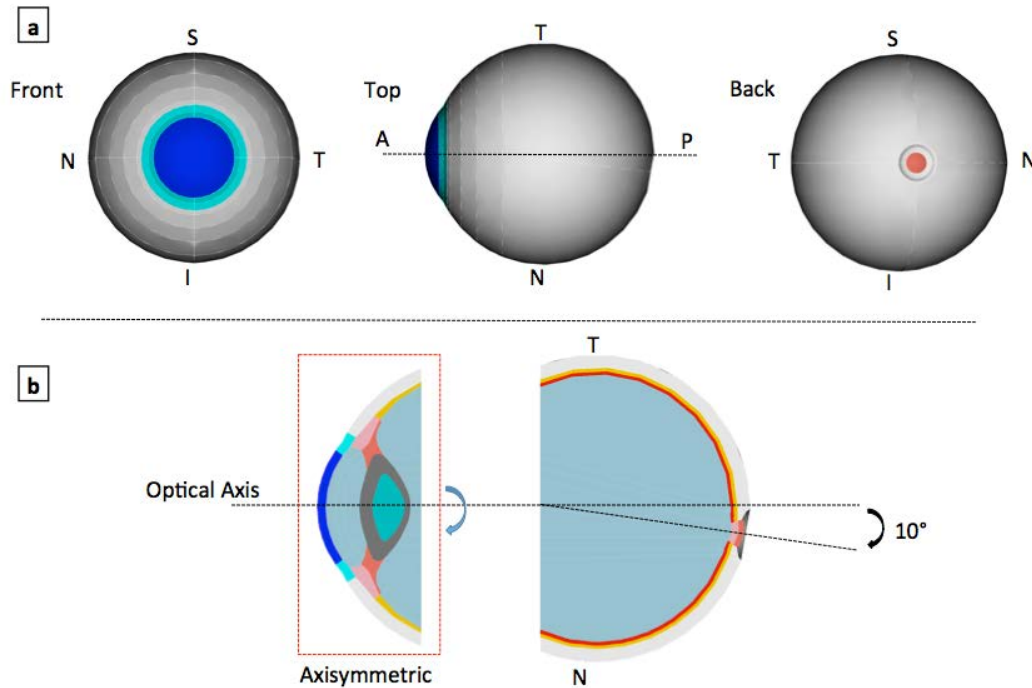


Fig. 9 Second-generation human eye model with offset ONH: a) different views of the model and b) shows model development by assuming symmetry about the optical axis for the anterior region only. In the posterior region, the ONH is offset approximately 10° in the nasal direction.

Other changes from the first- to second-generation model include increasing the uniform choroidal tissue thickness from 0.3 to 0.35 mm. This increase was based on measurements from Ikuno et al.⁴² of mean subfoveal choroidal thickness for healthy Japanese individuals with a mean age of 39 years. This update is shown in Fig. 10. The updated model also incorporates a prelaminar neural tissue (PLNT) component in the ONH. In the first-generation model, this region was approximated as a continuation of the retina. In the new model, the retina and choroid terminate at the scleral canal wall, meeting the PLNT. Posterior to the PLNT is the LC, as in the first-generation model. However, the thickness of the LC was increased in the new model from 0.3 to 0.45 mm.⁴³ The updated ONH, with inclusion of the PLNT component and the thicker LC, is shown in Fig. 11. The cup depth of the ONH was also modified in the second-generation model (Fig. 11). Many of these features have been coarsened to increase the mesh size and decrease the number of elements to help improve computational time.

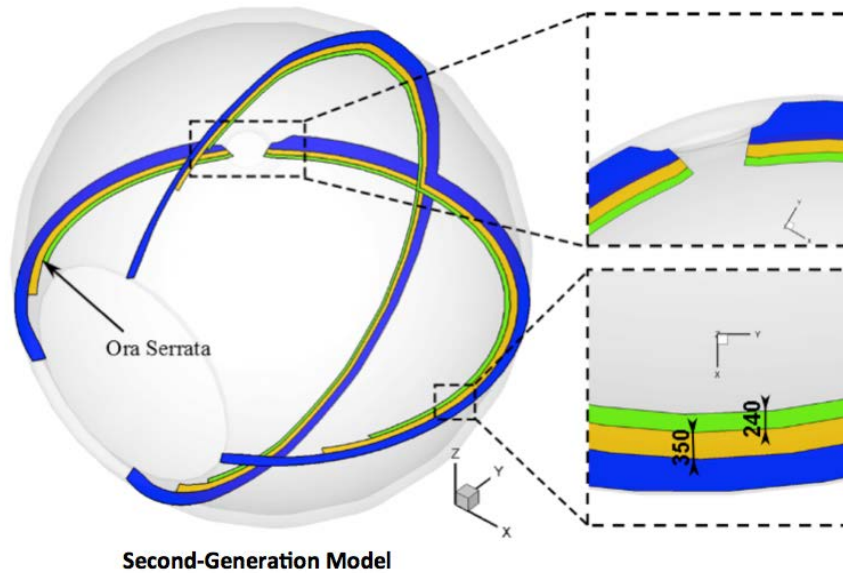


Fig. 10 Second-generation human eye model with offset ONH and updated choroidal thickness from 0.3 mm in the first-generation model to 0.35 mm⁴²

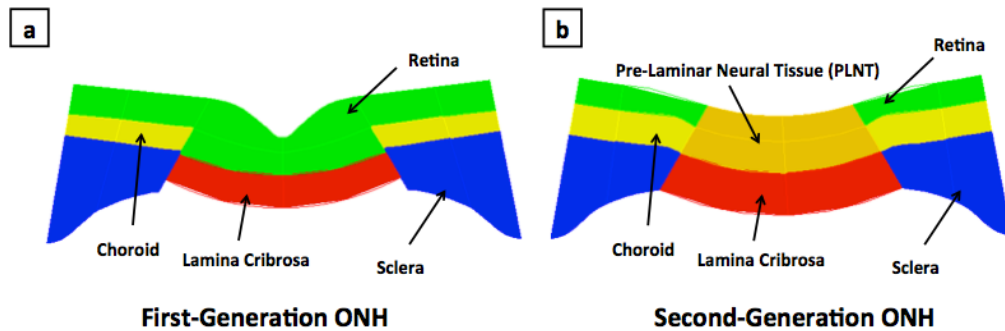


Fig. 11 Differences in the a) first and b) second-generation ONH models, including addition of a PLNT feature in the new model, an increased LC thickness from 0.3 to 0.45 mm, and a modified cup depth to increase element size and improve computational time

3. Scleral Thickness Variation

Comprising roughly 85% of the ocular shell, the fibrous scleral tissue plays a key role in helping to protect the eye from external loading and debris. In a blast-loading event, the highly pressurized blast wave can reflect off the bony facial features, shearing the ocular shell.²⁰ To accurately model the mechanical response of the tissues under such load, accounting for the change in scleral thickness across the entire globe may be necessary. The sclera varies in thickness from the anterior, where it meets the cornea at the limbus, to the posterior, where it terminates at the ONH, and quadrant to quadrant around the entire globe.

Norman et al.²⁴ performed a detailed experimental analysis on the variation of scleral thickness over the entire shell. MRI scans were analyzed from normal and glaucomatous human subjects. The images were sectioned into 15 equal-width sections along the anterior-posterior axis (12 sections for only the sclera) and divided into the 4 main quadrants (superior, inferior, nasal, and temporal), as shown in Fig. 12. Thickness measurements were obtained over 60 sections; approximately 150,000 total measurements per eye. They provided data for 48 total thickness measurements, as they only focused on the scleral tissue thickness variation in their study (select images shown in Figs. 12a and 12b). This data set included 12 measurements averaged over each section within each quadrant for all normal subjects.

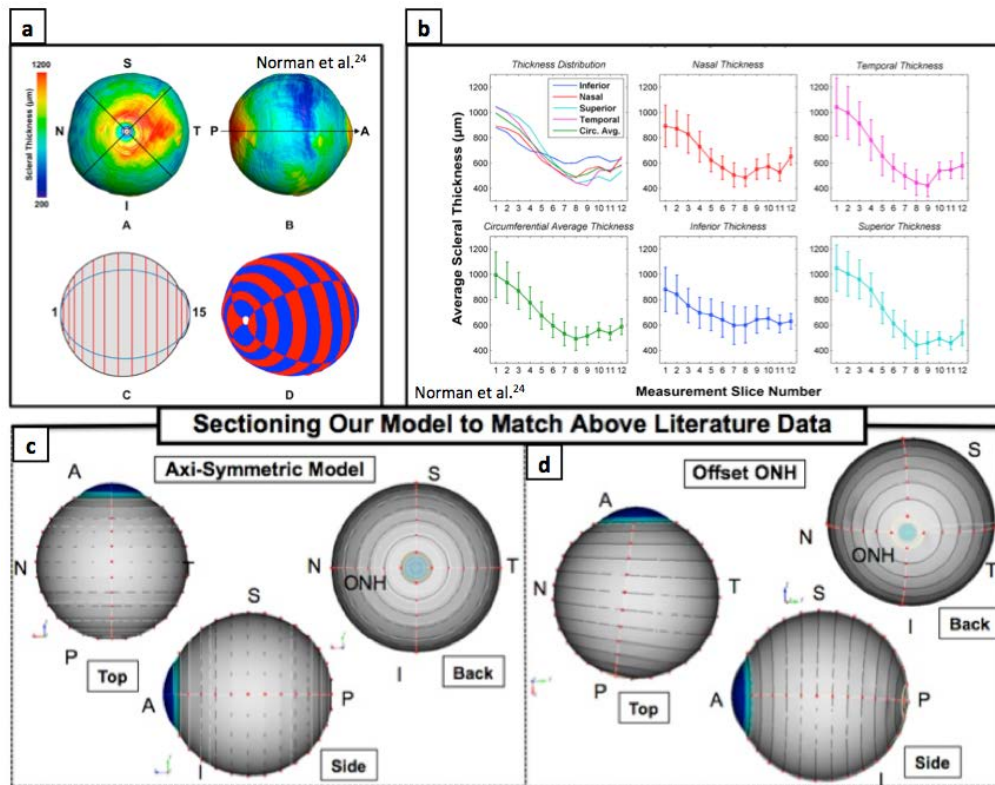


Fig. 12 Tissue thickness varies over the corneo-scleral shell, as shown in the literature.^{13,24} (a and b) A study conducted by Norman et al.²⁴ with images from normal human subjects sectioned into 15 equal-width sections along the anterior-posterior axis (12 sections of the sclera), and divided into 4 quadrants (60 total sections), over which thickness measurements were taken. (c) Our first-generation, axisymmetric model with 12 equal-width sections of the sclera (ONH to limbus). (d) Sectioning of the second-generation model where the ONH is offset to its geometrically accurate position.

We then implemented a code, developed in-house, to move all internal nodes of the scleral tissue to match the thickness of the sclera provided by Norman et al.^{3,24} for all 4 quadrants. The scleral thickness is defined on 4 peripheral points, at each

quadrant axis, and then linearly interpolated for intermediate points along sectoral planes from one quadrant to the next to ensure a coherent mesh (Fig. 13). Thicknesses at points on intermediate planes between each of the 12 slices were calculated through bilinear interpolation of the thickness at the 4 closest nodes. The outer scleral surface remains untouched. Local thickness was achieved by moving all nodes, aside from those on the outermost surface, either radially inward or outward depending on the original scleral thickness (1 mm) and the new desired thickness. Figure 13 shows thickness contours across the entire globe. Figure 13c demonstrates the procedure with before and after views of the scleral thickness variation. Because internal nodes of the sclera are connected to the choroid, which in turn are connected to the retina and vitreous humor, these nodes move accordingly to ensure thicknesses of the choroid and retina are not disturbed. This procedure is done in the same manner for both first- and second-generation models.

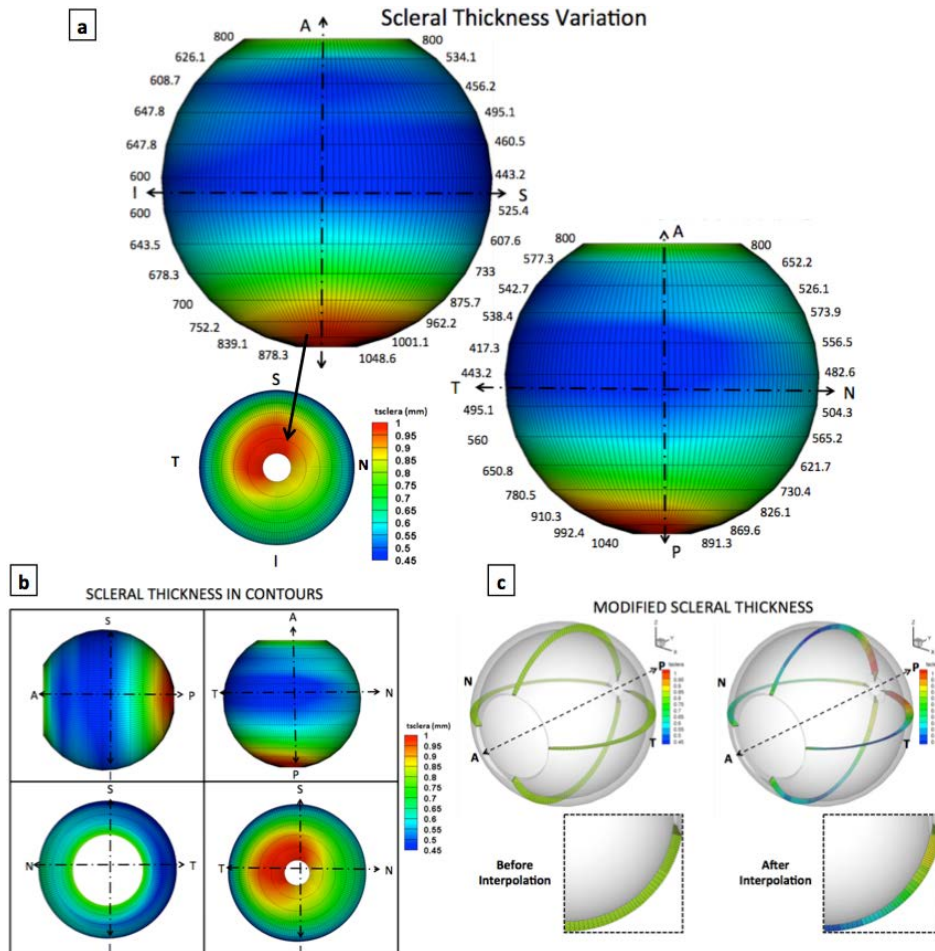


Fig. 13 Scleral thickness variation procedure in the model: a) scleral thickness variation contours with thickness values noted from Norman et al.,^{3,24} b) different views of scleral thickness variation contours, and c) views of the scleral thickness before and after interpolation was implemented

4. Conclusion

This report outlines the development of an anatomically accurate finite element model of the full human ocular globe with a surrounding extraocular orbital/tissue complex with means to fit securely within the skeletal orbit. This model was developed for use in fluid-structure interaction studies to assess blast-loading effects on the Soldier. The model does not include the iris, the macula and fovea pit, or individual extraocular muscles. The macula and fovea will be provided in a later model, as macular damage is a common effect of blast trauma. Extraocular muscles may be included as well to account for a more accurate rotation of the eye under the shearing loads applied from the blast event. To our knowledge, no model to date has incorporated such detailed intraocular components of the human eye, with an offset optic nerve head, while capturing scleral thickness variation spanning anterior to posterior and across all quadrants of the eye.

5. References

1. Sigal IA, Flanagan JG, Ethier CR. Factors influencing optic nerve head biomechanics. *Invest Ophthalmol Vis Sci*. 2005;46:4189–4199.
2. Downs JC, Roberts MD, Burgoyne CF, Hart RT. Multiscale finite element modeling of the lamina cribrosa microarchitecture in the eye. *Proc IEEE Eng Med Biol Soc*. 2009;2009:4277–4280. doi:10.1109/IEMBS.2009.5332755.
3. Norman RE, Flanagan JG, Sigal IA, Rausch SMK, Tertinegg I, Ethier CR. Finite element modeling of the human sclera: influence on optic nerve head biomechanics and connections with glaucoma. *Exp Eye Res*. 2011;93:4–12. doi:10.1016/j.exer.2010.09.014.
4. Sigal IA, Ethier CR. Biomechanics of the optic nerve head. *Exp Eye Res*. 2009;88(4):799–807. doi:10.1016/j.exer.2009.02.003.
5. Coudrillier B, Pijanka J, Jefferys J, Sorensen T, Quigley HA, Boote C, Nguyen TD. Effects of age and diabetes on the scleral stiffness. *J Biomech Eng*. 2015;137:071007.
6. Pijanka JK, Coudrillier B, Ziegler K, Sorensen T, Meek KM, Nguyen TD, Quigley HA, Boote C. Quantitative mapping of collagen fiber orientation in non-glaucoma and glaucoma posterior human scleras. *Investigative Ophthalmology and Vision Science*. 2012;53:5258–5270.
7. Coudrillier B, Pijanka J, Jefferys J, Goel A, Quigley HA, Boote C, Nguyen TD. Glaucoma-related changes in the mechanical properties and collagen micro-architecture of the human sclera. *PLOS One*. 2015;10:e0131396.
8. Nguyen TD, Ethier CR. Biomechanical assessment in models of glaucomatous optic neuropathy. *Exp Eye Res*. 2015;141:125–138.
9. Mohammad NT, Foster CD, Gongal D. Finite element modeling of cornea mechanics: a review. *Arq Bras Oftalmol*. 2014;77(1):60–65.
10. Carvalho LA, Prado M, Cunha RH, Neto AC, Paranhos A Jr, Schor P, Chamon W. Keratoconus prediction using a finite element model of the cornea with local biomechanical properties. *Arq Bras Oftalmol*. 2009;72(2):139–145. doi:10.1590/S0004-27492009000200002.
11. Liu X, Wang L, Wang C, Sun G, Liu S, Fan Y. Mechanism of traumatic retinal detachment in blunt impact: a finite element study. *J Biomech*. 2013;46:1321–1327.

12. Uchio E, Ohno S, Kudoh J, Aoki K, Kisielewicz LT. Simulation model of an eyeball based on finite element analysis on a supercomputer. *Br J Ophthalmol*. 1999;83(10):1106–1111. doi:10.1136/bjo.83.10.1106.
13. Stitzel JD, Duma SM, Cormier JM, Herring IP. A nonlinear finite element model of the eye with experimental validation for the prediction of globe rupture. *Stapp Car Crash Journal*. 2002;46:81–102.
14. Power ED. A nonlinear finite element model of the human eye to investigate ocular injuries from night vision goggles [thesis]. [Blacksburg (VA)]: Virginia Polytechnic Institute and State University; 2001.
15. Schutte S, van den Bedem SP, van Keulen F, van der Helm FC, Simonsz HJ. A finite-element analysis model of orbital biomechanics. *Vision Res*. 2006;46(11):1724–1731.
16. Watson R, Gray W, Sponsel WE, Lund BJ, Glickman RD, Groth SL, Reilly MA. Simulations of porcine eye exposure to primary blast insult. *Translational Vision Science & Technology*. 2015;4(8). doi:10.1167/tvst.4.4.8.
17. Rossi T, Boccassini B, Esposito L, Clemente C, Iossa M, Placentino L, Bonora N. Primary blast injury to the eye and orbit: finite element modeling. *Investig Ophthalmol Vis Sci*. 2012;53(13):8057–8066.
18. Esposito L, Clemente C, Bonora N, Rossi T. Modelling human eye under blast loading: computer methods in biomechanics and biomedical engineering. 2015;18(2):107–115. doi:10.1080/10255842.2013.779684.
19. Explosions and blast injuries: a primer for clinicians. Atlanta (GA): Centers for Disease Control (CDC) and Prevention [accessed 2016 22 Sep]. <http://www.cdc.gov/masstrauma/preparedness/primer.pdf>.
20. Bhardwaj R, Ziegler K, Seo JH, Ramesh KT, Nguyen TD. A computational model of blast loading on the human eye. *Biomech Model Mechanobiol*. 2014;13(1):123–140. doi:10.1007/s10237-013-0490-3.
21. Bailoor S, Bhardwaj R, Nguyen TD. Effectiveness of eye armor during blast loading. *Biomech Model Mechanobiol*. 2015;14:1227–1237.
22. Notghi B, Bhardwaj R, Bailoor S, Thompson KA, Weaver A, Stitzel J, Nguyen TD. Biomechanical evaluations of injury risk for blast loading. *Journal of Biomechanical Engineering*; 2016 Dec (submitted).
23. Cubit software, version 14.0. Used May–August 2013. <https://cubit.sandia.gov/>.

24. Norman RE, Flanagan JG, Rausch SM, Sigal IA, Terinegg I, Eilaghi A, Portnoy S, Sled JG, Ethier CR. Dimensions of the human sclera: thickness measurement and regional changes with axial length. *Exp Eye Res.* 2010;90:277–284.
25. Burd HJ. Numerical modelling of the accommodating lens. *Biomech Model Mechanobiol.* 2009;8:217–231.
26. Burd HJ, Judge SJ, Cross JA. Numerical modelling of the accommodating lens. *Vision Research.* 2002;42:2235–2251.
27. Hermans EA, Dubbelman M, van der Heijde GL, Heethaar RM. Estimating the external force acting on the human eye lens during accommodation by finite element modelling. *Vision Research.* 2006;46:3642–3650.
28. Schachar RA, Abolmaali A, Le T. Insights into the age-related decline in the amplitude of accommodation of the human lens using a non-linear finite-element model. *Br J Ophthalmol.* 2006;90:1304–1309.
29. Lanchares E, Navarro R, Calvoa B. Hyperelastic modelling of the crystalline lens: accommodation and presbyopia. *Journal of Optometry.* 2012;5:110–120.
30. Bernal A, Parel JM, Manns F. Evidence for posterior zonular fiber attachment on the anterior hyaloid membrane. *Invest Ophthalmol Vis Sci.* 2006;47:4708–4713.
31. Kao C-Y, Richdale K, Sinnott LT, Ernst LE, Bailey MD. Semi-automatic extraction algorithm for images of the ciliary muscle. *Optom Vis Sci.* 2011; 88(2):275–289.
32. Sigal IA, Flanagan JG, Tertinegg I, and Ethier CR. Finite element modeling of optic nerve head biomechanics. *Invest Ophthalmol Vis Sci.* 2004;45:4378–4387.
33. Asrani S, Zou S, d’Anna S, Vitale S, Zeimer R. Noninvasive mapping of the normal retinal thickness at the posterior pole. *Ophthalmology* 1999;106:269–273.
34. Chan A, Duker JS, Ko TH, Fujimoto JG, Schuma JS. Normal macular thickness measurements in healthy eyes using stratus optical coherence tomography. *Arch Ophthalmol.* 2006;124(2):193–198.
35. Landau D, Schneidman EM, Lacobovitz T, Rozenman Y. Quantitative in vivo retinal thickness measurements in healthy subjects. *Ophthalmology* 1997;104:639–642.

36. Wagner-Schuman M et al. Race- and sex-related differences in retinal thickness and foveal pit morphology. *Investigative Ophthalmology & Visual Science*. 2011;52(1):625–634.
37. Manjunath V, Taha M, Fujimoto JG, Duker JS. Choroidal thickness in normal eyes measured using cirrus-HD optical coherence tomography. *Am J Ophthalmol*. 2010;150(3):325–329.
38. Yi K, Mujat M, Sun W, Park BH, de Boer JF, Chen TC. Peripapillary retinal thickness maps in the evaluation of glaucoma patients: a novel concept. *ISRN Ophthalmology*; 2011. Article ID No.: 146813. doi:10.5402/2011/146813.
39. Roberts KF, Artes PH, OLeary N, Reis AS, Sharpe GP, Hutchison DM, Chauhan BC, Nicolela MT. Peripapillary choroidal thickness in healthy controls and patients with focal, diffuse, and sclerotic glaucomatous optic disc damage. *Arch Ophthalmol*. 2012;130(8):980–986.
40. Chairman WN. Optics of the human eye. In: Cronly Dillon J, editor. *Visual optics and instrumentation*. Boca Raton (FL): CRC Press; 1991. p. 1–26.
41. Rohrschneider K. Determination of the location of the fovea on the fundus. *Invest Ophthalmol Vis Sci*. 2004;45(9):3257–3258.
42. Ikuno Y, Kawaguchi K, Nouchi T, Yasuno Y. Choroidal thickness in healthy Japanese subjects. *Invest Ophthalmol Vis Sci*. 2010;51:2173–2176. doi:10.1167/iovs.09-4383.
43. Jonas JB, Berenshtein E, Holbach L. Lamina cribrosa thickness and spatial relationships between intraocular space and cerebrospinal fluid space in highly myopic eyes. *Invest Ophthalmol Vis Sci*. 2004;45:2660–2665.

List of Symbols, Abbreviations, and Acronyms

2-D	2-dimensional
3-D	3-dimensional
LC	lamina cribrosa
MRI	magnetic resonance imaging
ONH	optical nerve head
PLNT	prelaminar neural tissue

1 DEFENSE TECHNICAL
(PDF) INFORMATION CTR
DTIC OCA

2 DIRECTOR
(PDF) US ARMY RESEARCH LAB
RDRL CIO L
IMAL HRA MAIL & RECORDS
MGMT

1 GOVT PRINTG OFC
(PDF) A MALHOTRA

3 JOHNS HOPKINS UNIV
(PDF) T D NGUYEN
B NOTGHI
S BAILOOR

1 INDIAN INST OF TECHLGY
(PDF) R BHARDWAJ

11 NATICK SOLDIER RSRCH
(PDF) DEV AND
ENGRNG CTR
M G CARBONI
D COLANTO
R DILALLA
J FONTECCHIO
B KIMBALL
J KIREJCZYK
M MAFEO
M MARKEY
J PARKER
D PHELPS
J WARD

3 PROG EXECUTIVE OFC
(PDF) SOLDIER
A FOURNIER
J MULLENIX
J ZHENG

5 SOUTHWEST RSRCH INST
(PDF) C ANDERSON JR
S CHOCRON
D NICOLELLA
T HOLMQUIST
G JOHNSON

1 INST FOR DEFNS ANLYS
(PDF) Y MACHERET

1 US ARMED FORCES
(PDF) MEDICAL
EXAMINER SYS
J GETZ

4 MRMC DOD BLAST INJURY
(PDF) RSRCH
PROG COORDINATING OFC
R GUPTA
M LEGGIERI
R SHOGE
S HINDS

1 WIAMAN PMO
(PDF) S MARSH

3 MRMC JTAPIC PRGM OFC
(PDF) F LEBEDA
W LEI
J USCILOWICZ

3 US ARMY AEROMEDICAL
(PDF) RSRCH LAB
V CHANCEY
B MCENTYRE
D WISE

1 TARDEC
(PDF) R SCHERER

1 RDECOM HQ
(PDF) AMSRD PE
D RUSIN

44 DIR USARL
(PDF) RDRL SLB W
J GURGANUS
J IVANCIK
W MERMAGEN
K RAFAELS
RDRL WM
S SCHOENFELD
RDRL WMM
M VANLANDINGHAM
RDRL WMM A
D O'BRIEN
T PLAISTED
E WETZEL

RDRL WMM B
T BOGETTI
B LOVE
P MOY
C YEN
RDRL WMM D
B CHEESEMAN
S WALSH
RDRL WMM E
L VARGAS-GONZALEZ
RDRL WMP B
A DAGRO
A DILEONARDI
A EIDSMORE
A GUNNARSSON
C HAMPTON
C HOPPEL
Y HUANG
M KLEINBERGER
J MCDONALD
P MCKEE
S SATAPATHY
A SOKOLOW
K THOMPSON
T WEERASOORIYA
S WOZNIAK
T ZHANG
RDRL WMP C
R BECKER
T BJERKE
RDRL WMP D
C RANDOW
R DONEY
B SCOTT
RDRL WMP E
S BARTUS
M BURKINS
P GILLICH
M LOVE
P SWOBODA
RDRL WMP F
N GNIAZDOWSKI
R GUPTA